Journal Name

ARTICLE

Selective Delivery of Photothermal Nanoparticles to Tumors Using Mesenchymal Stem Cells as Trojan Horses

Received 00th January 20xx,
Accepted 00th January 20xx

DOI: 10.1039/x0xx00000x

www.rsc.org/

M. Mar Encabo-Berzosa[a,b,c], Marina Gimeno[d], Lluis Lujan[d], Maria Sancho-Albero[a,b] Leyre Gomez[a,b], Victor Sebastian[a,b], Miguel Quintanilla[e], Manuel Arruebo[a,b,§], Jesus Santamaria[a,b], Pilar Martin-Duque[c,f,g,§]

The main challenge of cancer treatment is to avoid or minimize systemic side effects in off-target tissues. Mesenchymal stem cells (MSCs) can be used as therapeutical carriers because of their ability to migrate and incorporate into inflammation areas including tumors. Here, this homing ability is exploited by carrying therapeutic nanoparticles (Hollow Gold Nanoparticles (HGNs)) following a "Trojan-horse" strategy. Amongst the different nanoparticles to be employed, HGNs have the capacity to resonate in the near infrared region when irradiated by an appropriated laser (808 nm). By transforming this absorbed energy into heat, they are capable to produce locally induced hyperthermia. At this wavelength healthy tissues have a minimal light absorption being the effect restricted to the tissues containing HGNs. By placing HGNs inside MSCs, the recognition, excretion and immune response are minimized. We demonstrate that MSCs internalize HGNs and reach the tumors still containing HGNs. After laser treatment this loaded cells are able to eradicate tumoral cells *in vitro* and *in vivo* without significant toxicity. Also Ki67 expression, which is usually correlated with proliferation, is reduced after treatment. This approach enhances the effectiveness of the treatment when compared to just the enhanced permeation and retention effect (EPR) of the HGNs by themselves.

Introduction

Cancer is the leading cause of death worldwide, with 7.6 million deaths in 2013; data which are projected to continue rising with an estimated 13.1 million deaths in 2030 according to WHO.[1] The increase in the life expectancy, the presence of mutagenic agents in the environment, and the lack of healthy habits could influence this high incidence of the disease.[2]

Preventive medicine, surgery, chemotherapy and radiotherapy are the main approaches to defeat cancer, but the three latter therapeutical approaches have major side effects because they affect both tumoral and healthy tissues. Therefore, there is a need to develop new, more effective and safer treatments able to reach homogeneously all the tumoral mass, including the central hypoxic regions.

One of the nano-based emerging therapies proposed in recent years involves the generation of hyperthermia or tumoral ablation using either magnetic or near-infrared (NIR) responsive nanoparticles which are able to generate localized heat by the use of alternating magnetic fields or NIR light, respectively. In this particular application, phototherapy consists on an increase in the local temperature by using the heat transmitted by the NIR-absorbing nanoparticles upon laser irradiation, leading to the apoptosis or necrosis of the tumoral cells depending on the laser fluence, pulse frequency, wavelength of the irradiating light and exposure time. Specifically, gold nanoparticles are good candidates to mediate in this process because of their high light absorption efficiency, low cytotoxicity at the doses used, good biocompatibility and

[a] Department of Chemical Engineering. Aragon Nanoscience Institute (INA), University of Zaragoza, Spain
[b] CIBER de Bioingeniería, Biomateriales y Nanomedicina, CIBER-BBN, Zaragoza, Spain
[c] Instituto Aragonés de Ciencias de la Salud (IIS Aragon), Centro de Investigación Biomédica de Aragón (CIBA), Zaragoza, Spain
[d] Department of Animal Pathology, Veterinary Faculty, University of Zaragoza, Spain
[e] Instituto de Investigaciones Biomédicas "Alberto Sols", Madrid, Spain
[f] Universidad Francisco de Vitoria, Facultad de Ciencias Biosanitarias, Madrid, Spain
[g] Fundación Araid, Zaragoza, Spain
† Footnotes relating to the title and/or authors should appear here.
Electronic Supplementary Information (ESI) available: [details of any supplementary information available should be included here]. See DOI: 10.1039/x0xx00000x

their simple and scalable synthesis.[3] Hollow gold nanoparticles (HGNs) are able to absorb energy in the NIR region of the electromagnetic spectrum and dissipate it as heat due to electron-electron and electron-phonon relaxations. Between 650 and 1100 nm the absorption and scattering of incident light in biological tissues are minimized due to the reduced absorption by water and chromophores. In this way, external irradiation of tissues with single wavelength lasers in this region (i.e. 808 nm) under a controlled irradiance (usually below 200mW/cm^2) produces heat only where the light absorbing nanoparticles are embedded, reducing the characteristic side effects of other conventional treatments such as chemo- or radiotherapy and to other hyperthermia based techniques such as microwave ablation, magnetic fluid ablation, radiofrequency, and focused ultrasound therapy.[2] Compared to other plasmonic nanoparticles such as gold nanorods or core-shell SiO_2-Au nanoshells, HGNs are more efficient in photothermal therapy for shallow and deep cancers.[4] However, even though there are very efficient transductors of the NIR light into heat, the use of generalized hyperthermia also produces damage in healthy cells and tissues, and therefore, it is important to obtain local hyperthermia exclusively at the tumor site which is by no means an easy task.[5] The well-known enhanced permeation and retention (EPR) effect and a defective lymphatic drainage contribute to the passive over-accumulation of nanoparticles at the tumor[6] but experimental patient data corroborating this mechanism are reduced.[7] Selective accumulation can be further increased by the use of suitable antibodies or other recognition biomolecules (carbohydrates, peptides, aptamers, etc.) grafted to the external nanoparticle surface.[8] However, a selective accumulation of nanoparticles requires sufficient circulation time in the bloodstream, but, as it is well known, after protein adsorption on their surfaces, nanoparticles are rapidly cleared from circulation by the macrophages of the reticulo-endothelial system[9] and by the inherent filtration ability of the liver and the spleen.[10] To reduce protein adsorption, stealthing strategies (e.g. by coating with layers of poly-ethylene glycol, with biomimetic surface modifications using phosphatidylcholine, or with self-membrane proteins, etc.) have been developed to increase their circulation life time by mimicking cell´s glycocalyx.[9,10] In addition, nanoparticles can also be delivered using cells as carriers to evade the immune system recognition ability, in a so-called "Trojan horse" strategy.

This concept of Trojan horse has been postulated in previous works using different nanoparticle-laden cells including dendritic[11], macrophages[12–14] and T lymphocytes.[15]

Kang et al.[16] have recently demonstrated that pH-sensitive gold nanoparticles can be loaded within MSCs and be administered intravenously showing a 37 fold increase in the tumor targeting efficacy compared to the administration of free nanoparticles which resulted in a significantly enhanced photothermal effect. However, in this work, the excitation wavelength used (660 nm) shows a limited penetration in the tissues, and a higher melanin and haemoglobin absorption compared to NIR wavelengths (i.e., 808 nm). In addition, three consecutive nanoparticle loading doses (50 μg/mL) were administered to the MSCs to reach enough nanoparticle-loading to produce an efficient photothermal effect. However, in this work we prepare nanoparticles optimized for light absorption from a higher penetration 808 nm laser source and optimize the loading of HGNs in MSCs. In this way we are able to obtain an improved outcome using a lower nanoparticle loading (just 1 single dose of 50 μg/mL). We also used PEG-coated nanoparticles in order to reduce bioaccumulation and potential subsequent toxicity in off-target organs and also to make a meaningful comparison between the results obtained by systemic delivery of HGNs (EPR effect) and by the Trojan horse strategy pursued in this work.

Also, Liu et al[17] have developed a cell based method in order to accumulate NPs in tumors. In their work, gold nanorods functionalized with CXCR4 were loaded into induced pluripotent stem cells (iPS cells). However, it is know that intravenous injection of iPS in mice with primary tumors highly promoted tumor growth[18] and also the formation of teratomas is a serious risk associated with iPS intravenous injection[19]. In addition, they assume the death of iPS embedded in tumors after NPs mediation hyperthermia by laser irradiation. As the authors mentioned, a percentage of the NPs were released by the cells, therefore a risk of tumoral escape of un-loaded iPS exits. They also showed that a small part of injected iPS was accumulated in liver and lungs.

In comparison with those previous vectors, bone marrow MSCs have a number of characteristics that make them superior, including their ability for self-renewal, potential to differentiate into different tissues and ability to migrate and integrate at sites of inflammation or into tumors.[18,20,21] Although the complete mechanism of this phenomenon is still unknown, it is recognized that the release of cytokines in the tumor stroma and their interaction with cytokine and chemokine receptors present on the cell surfaces are involved in the migration of MSCs as well as the intra-tumoral hypoxic environment which does not impair their migration.[22] This homing ability is currently used in clinical trials using patient derived mesenchymal stem cells as virus carriers in the treatment of ovarian cancer.[23] Nanoparticle transport inside MSCs directed against brain tumors was previously demonstrated, although, in that case MSCs were directly injected on site, being the MSCs observed afterwards in the tumor periphery.[24] Dwyer et al.[25] demonstrated a successful engraftment of MSCs at the site of both primary tumors and nodal cancer metastases after systemic administration *in vivo*, although no nanoparticle was carried in that case.

Moreover, MSCs present a great advantage in relation to solve some of the problems found during the nanoparticle-based injection alone such as the previously mentioned rapid immune response and low permeance of free nanoparticles towards the interior of the tumoral mass due to the high pressure gradient. Regarding the immune response, the fact that they do not express MHC class II and have a very low expression of MHC class I,[22,26] may favour the use of these cells in allografts. As it is also known that bone marrow MSCs are able to migrate to hypoxic areas,[22] here we propose the

use of these cells as vectors for NIR-responsive nanoparticles to delivery treatment to the central hypoxic areas of tumors by applying NIR hyperthermia.

Results and discussion

Nanoparticle physic-chemical and biological characterization. Spherical hollow gold nanoparticles with 40.5 ± 7 nm in diameter (Figure 1a-c), were obtained after galvanic replacement using cobalt oxide nanoparticles as templates. Both HGNs and PEG-HGNs showed a characteristic localized surface plasmon resonance peak in the NIR region (Figure 1d). A slight blue shift was observed for the pegylated nanoparticles, possibly attributed to a different dielectric value in the interfacial double layer coating the nanoparticles in agreement with the previous literature[27]. The amount of PEG on the surface of the HGNs was 12 µg·g-1, evaluated by TGA.

Compared to the control, PEG-HGNs did not decrease the cell viability at all the doses tested (20, 50, 100 and 500 µg·mL-1) (Figure 2a). Our results are in agreement with previous studies

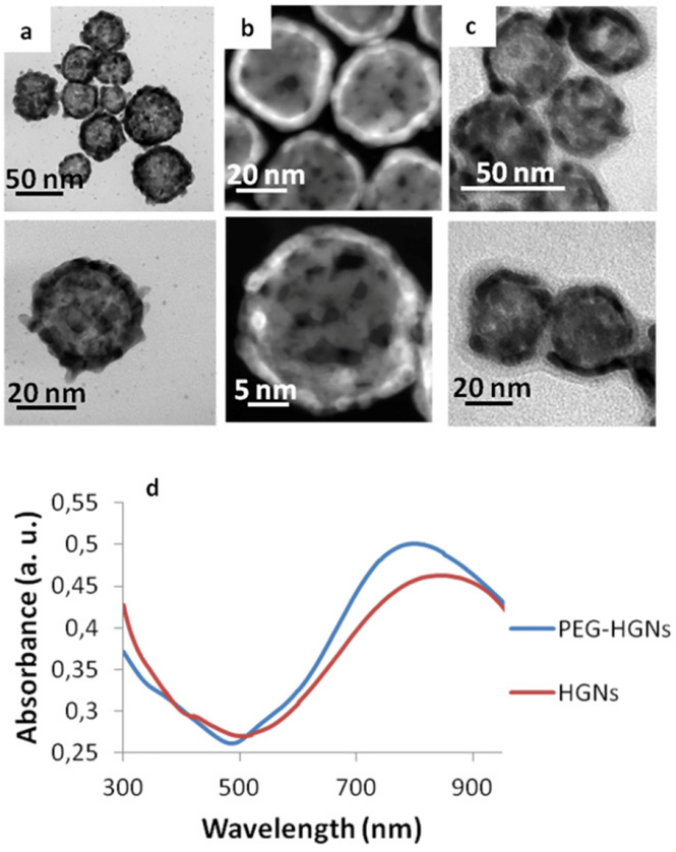

Figure 1. Characterization of the photothermal nanoparticles (a) TEM images for Hollow Gold Nanospheres. (b) STEM-HAADF images. (c) TEM images of PEG-Hollow Gold Nanospheres. The halo around the nanoparticles demonstrates the PEG coating. In this case, phosphotungstic acid was used to dye the polymeric corona and allow TEM observation. (d) UV-Vis extinction spectra of HGNs and PEG-HGNs.

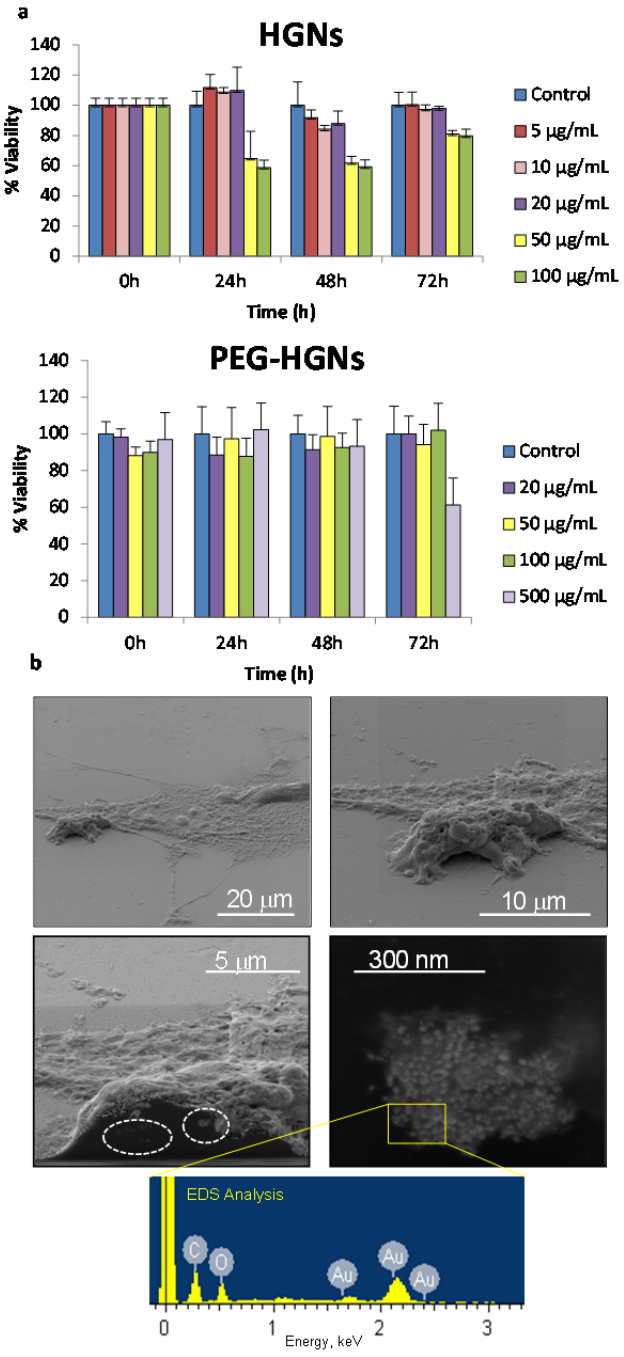

Figure 2. Cytotoxicity and cell trafficking studies (a) Graphs showed AlamarBlue assays results for bare HGNs and PEG-coated HGNs (PEG-HGNs), respectively. For the experiments with HGNs, 20 µg·mL^{-1} was chosen as the highest dose which did not induce cytotoxicity. For the PEG-HGNs 50 µg·mL^{-1} was chosen as limit for the sub-cytotoxic dose. (b) SEM Dual Beam images demonstrate that the nanoparticles are located inside the cells. The two images above correspond to a HGN-laden-MSC at different magnifications. In the bottom left image a cross section of the same cell shows the presence of internal agglomerated HGNs, the zoom showed in the right panel shows the morphology of those aggregates. EDX analysis on those aggregates corroborated the presence of Au inside the cell.

which demonstrate that nanoparticle cytotoxicity is reduced after pegylation.[28] Also, this reduced cytotoxicity for MSCs harboring HGNs is in agreement with previous reports[29]. In

contrast, a dose-dependent cytotoxicity was observed for the bare HGNs with a marked decrease in the cell viability at doses above 50 µg mL-1 after 24h of incubation in agreement with the previous literature[30]. It is important to point out that the apparent increase in cell viability observed after 72h of incubation is just caused by the use of the total number of viable cells remaining after 72 h as control. To distinguish the cell death pathways a LIVE/DEAD® test was performed (see supporting information Figure SI1).

Nanoparticle cell trafficking was evaluated by using confocal microscopy, scanning electron microscopy, flow cytometry and ICP. HGNs internalization was also demonstrated by using SEM Dual-Beam that allowed examination of the cell interior after being sectioned by the focused ion beam (Figure 2b). For the confocal studies, cells were permeabilized and stained with Draq5 to label the nuclei and with phalloidin-Alexa488 to stain the cytoskeletal actin fibers. Due to their agglomeration in endocytic vesicles, HGNs were observed by using the reflection mode of the microscope exciting at 488 nm and collecting the emission between 479 and 498 nm. Z-stack orthogonal projections were carried out in order to demonstrate the presence of the nanoparticles inside the cytosol (Figure 3).

Nanoparticles were clearly internalized forming aggregates inside vesicles, probably following the endosomal route, and the gene expression was observed even after 7 days of co-incubation (see Supporting Information Figure SI2). Even EDX analysis on internalized aggregates corroborated the presence of Au inside the cells. Differences in the internalization dynamics were found using flow cytometry by labelling the bare and PEGylated nanoparticles with rhodamine123. A maximum nanoparticle loading was reached at 24 and at 72 hours for the PEG-HGNs and the HGNs, respectively. Using UVVIS spectrophotometry we calculated the amount of internalized PEG-HGNs and we obtained a dose of $1.2.10^{-6}$ mg of nanoparticles per cell after 24 h of incubation. It is important to point out that the chemical bond (Au-N) between rhodamine123 and gold through the lone pair electrons at the amino groups discards the potential detachment of the dye from the nanoparticles[31]. The differences in the loading kinetics may be attributable to the differences in the dynamics of the endocytic-exocytic route. This internalization process is dynamic and part of the endocyted nanoparticles are exocytosed following the lysosomal route, but those particles could be newly internalized within another MSC (see Supporting information Figure SI3 where live cell imaging was performed). In any case, while at a given time-point the amount of internalized nanoparticles may vary, our results clearly indicate (Figure SI2) that internalized nanoparticles are present within the MSCs for several days after incubation, allowing time for their migration to tumor sites. In addition, in agreement with Kang et al.[16], the presence of agglomerates within endosomes such as those found in figures 2 and 3 reduces gold

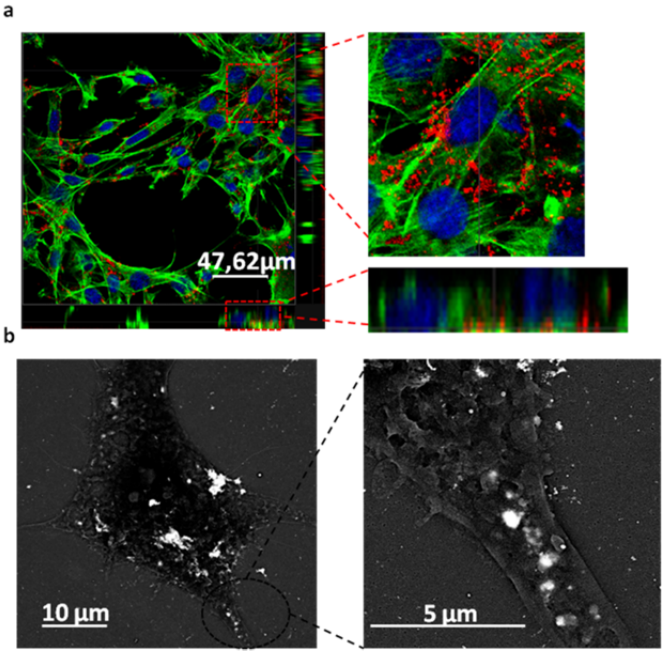

Figure 3. Nanoparticle internalization within MSCs. (a) Confocal Z-Stack. Red dots correspond to the labelled HGNs in the cell after 24 h of incubation with PEG-HGNs. The inset shows that red labelled nanoparticles are surrounded by green actin fibers (b) SEM backscattered image highlighting the presence of the gold nanoparticle agglomerates within the cells. EDX corroborated that the atomic composition of those aggregates corresponded to gold (results not shown).

nanoparticle exocytosis enhancing cellular retention. They showed how large internalized nanoparticle agglomerates (>200 nm) remained inside the MSC endosomes after 24h of incubation and, in our work, we showed that even larger sizes (Figure 2b) were achieved inside the MSCs when using HGNs as photothermal transducers.

***In vivo* photothermal studies**. In the intratumoral injection (first) experiment, the treated groups were injected either with 50 µg of HGNs or with one million of MSCs co-incubated with 50 µg of HGNs during 72h. Tumors in Group 5 (HGNs+laser) reduced completely their sizes one week after irradiation (Figure 4). This result reflects the efficiency of the plasmonic HGNs in releasing heat locally when subjected to NIR irradiation. Since in this experiment, the HGNs were injected stereotactically, they are expected to be located inside or in the close proximity of the tumor. Tumor sizes in Group 4 (MSCs + HGNs +laser) strongly decreased (~ 80% reduction in the projected area by day 12), but the tumor reduction was not as high as the one observed for Group 5. This is likely due to the lower dose (ca. 33wt.% less) of plasmonic nanoparticles transported by the MSCs since although the total HGN amount used for incubation (50 µg) is the same as that injected in group 5, about one third of the particles are not internalized (data not shown), and are

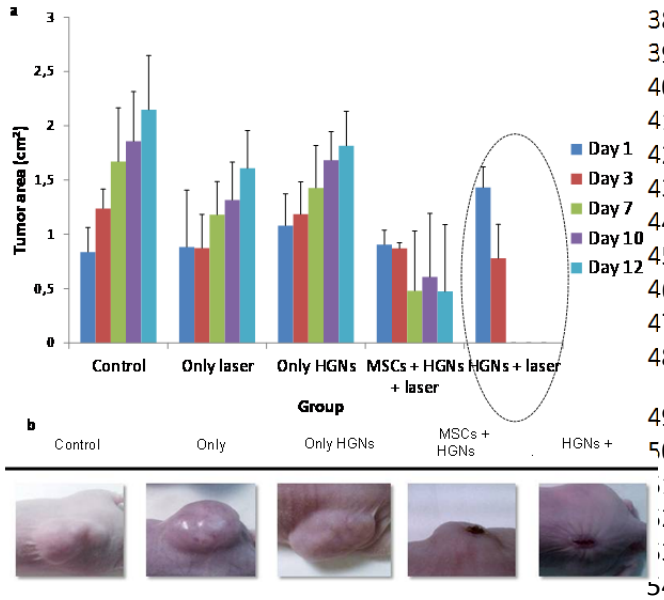

Figure 4. Photothermal therapy on HeLa cell-line xenograft tumors after intratumoral administration in vivo. (a) Tumor size evolution over time for both treated and control groups. (b) Photographs of HeLa xenografts at day 12 after laser irradiation (1W.cm^{-2} during 5 min). It is worth noting that the projected laser-spot size was larger than the size of the projected area of the tumors, i.e., the whole tumor area was irradiated at the same time.

removed during washing. In all other control groups tumor sizes increased. Figure 4a shows the evolution of the projected area of the tumor over time. Our results show that NIR hyperthermia reduces the size of the tumor in only one week after treatment when a direct intra-tumoral injection was used whereas, in other works, the combined use of intravenously administered NIR-responsive nanoparticles and chemotherapy produced also a complete tumor remission 20 days after irradiation[32]. Therefore, the route of administration plays a key role in the dynamic process of over-accumulating a therapeutic dose of plasmonic nanoparticles in the tumoral area and also depends on the tumor model. Obviously in a localized and accessible tumor a direct intratumoral injection of the plasmonic nanoparticles would be enough to achieve a complete tumoral eradication. However, for non-localized tumors or tumors in their early stages that are still too small to be detected the use of intravenously administered targeting nanoparticles would be a benefit. In this regard, in a second experiment (Figure 5) and after the demonstration that HGNs were able to mediate tumor regression, we administered the nanoparticles via intravenous injection in the corresponding mouse. In this case, in order to reduce the number of animals we divided the animals into four groups. The control groups included the use of MSCs containing PEG-HGNs but without any laser application and one additional control group without any treatment. We either used PEG-HGNs or MSCs harboring PEG-HGNs in the other two experimental groups. As mentioned before, MSCs can migrate to sites of injury and inflammation[18], so we used these cells intravenously to analyze their capability to over-accumulate sub-cytotoxic doses of plasmonic nanoparticles in hypoxic and inflamed diseased tissues. Instead of bare HGNs, PEG-HGNs were used and delivered to tumors since these would be used in a hypothetical EPR application in order to reduce the recognition and fast clearance of the bare nanoparticles by the immune system. In this experiment we used U251MG glioma cells as a model tumor, because of the aggressiveness of this malignant tumor, which represents a greater challenge than the previous HeLa-based model used in the first experiment.

All groups were injected with 5 x 10^6 U251MG cells in one flank of the mouse for tumor induction. In this case, the weight of the PEG corona must be taken into account. Therefore, to have a similar amount of gold as in the previous experiment we injected in the tail of the mouse a higher dose of PEG-HGNs (100 µg per animal) or one million MSCs per animal incubated with 100 µg PEG-HGNs. In this case, one day after the injection, tumors were irradiated. At this time point, before irradiation, a dark staining at the tumor site was discernible where PEG-HGNs were used, while this was not observed for

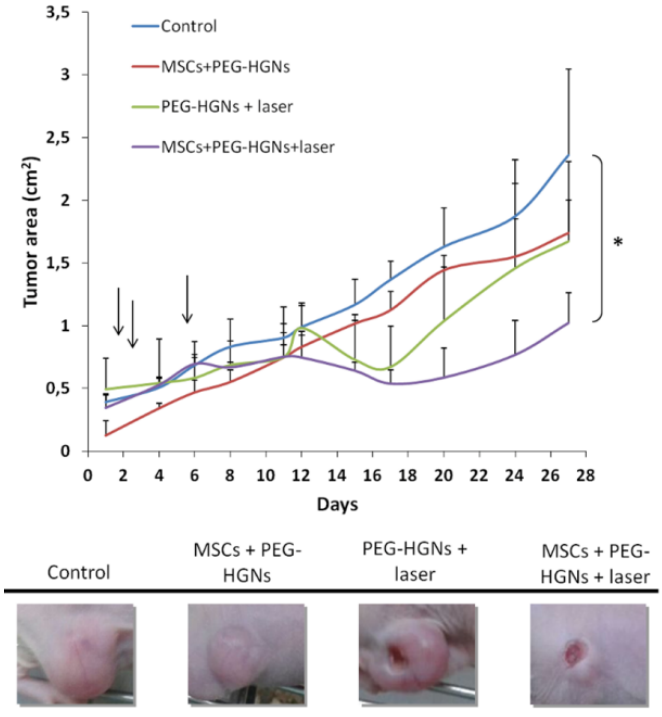

Figure 5. Photothermal therapy on U251MG cell-line xenograft tumors after intravenous administration. (a) Tumor size evolution over time for both treated and control groups. The first arrow indicates the time in which HGNs or HGNs-loaded in MSCs were administered, the second and the third arrows show the time span in which the laser irradiation took place. The difference between control and the group marked with * were statistically significant ($p<0.05$) (b) Photographs of U251MG xenografts at day 12 after the first laser irradiation.

the control group. This indicates that part of the PEG-HGNs had already reached the tumor probably due to the EPR effect, in agreement with previous works using dynamic imaging studies in which it was demonstrated that metal nanoparticles accumulate immediately in the tumor *in vivo*[33,34]. One week after the intravenous injection we irradiated the tumors again, because, as it was previously reported, it takes approximately one week for bone marrow MSCs to accumulate in the tumoral area[35].

Tumor development was followed until mice carried tumors at the ethically allowed size. At the end of the experiment the size of the tumors in the group with MSCs + PEG-HGNs and laser irradiation showed a higher decrease in the projected area compared to the group treated with just PEG-HGNs and irradiated laser without Trojan cells as carriers. This suggests that MSCs have been able to carry the nanoparticles to the tumors more efficiently than the well-known extravasation achieved thanks to the EPR effect when using free nanoparticles. The heterogeneity of the EPR effect in human cancers, and the uncertainty regarding the intensity of its effect in clinical cases has been widely reported in the literature[36] although experimental patient data corroborating its therapeutic mechanism are reduced[7]. Our results are in agreement with the work of Zhang et al.[29] who demonstrated a co-localization of human MSCs loaded with HGNs around tumoral blood vessels. Between the control group and the group treated with loaded MSCs and laser the differences in the tumor projected area at the end of the experiment were statistically significant ($p<0.05$). In the group with MSCs + PEG-HGNs without laser no significant differences were observed in the total tumor projected area compared to the one measured for the control. Smith et al.[36] have recently reported how intravenously administered carbon nanotubes might be uptaken by a specific subset of circulating inflammatory monocytes which carry them into the tumor. This means that in the case of free PEG-HGNs in addition to extravasation and accumulation due to the EPR a monocyte-based transport might also be contributing to HGN accumulation. However, the reported ability of MSCs to engraft in the tumoral stroma would likely deliver higher doses of therapeutic nanoparticles in the target. To corroborate this aspect, histological studies were carried out on the tumors (Figure 6).

Histological and immunohistochemical analysis. The histological studies demonstrated that all the tumors showed an expansive, non-encapsulated, highly cellular neoplastic proliferation composed of extensive sheets of polyhedral highly pleomorphic cells with atypical mitosis. Tumor cells showed round to ovoid nuclei, prominent nucleoli and a moderated, ill-defined eosinophylic cytoplasm. In those cells the stroma was formed by a scant connective tissue.

As shown in Figure 6, all groups (B1-B4) exhibited tumor masses with a central necrotic area. Interestingly, whereas B1 (control) and B4 (MSCs + PEG-HGNs without laser) tumors presented a single central area of necrosis, B2 (PEG-HGNs + laser) and B3 (MSCs + PEG- HGNs with laser) tumors showed additionally extensive multifocal necrotic areas within peripheral, viable tumor parenchyma. Regarding the mitotic activity index, B1 and B4 tumors showed a mean of 15 mitotic figures/10 HPF whereas the mean for B2 and B3 tumors was 9 mitotic figures/10 HPF. Globally, these results corroborate the efficiency of treatment using photothermal nanoparticles combined with laser irradiation.

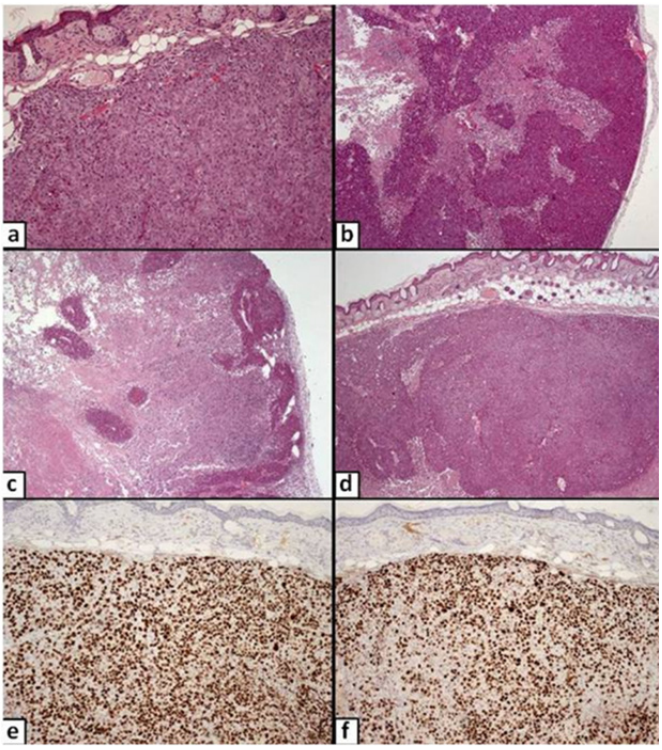

Figure 6. Hematoxylin-eosin staining results for histological sections recovered at the end of the experiment. (a-d). Ki-67 staining (e-f). (a) Control tumor (B1 group). Highly cellular pleomorphic neoplastic proliferation. H&E 10x. (b) PEG-HGNs+ laser treated tumor (B2 group). Multifocal necrotic areas on the tumor parenchyma. H&E 4x. (c) MSCs+ PEG-HGNs+ laser treated tumor (B3 group). Focally extensive necrotic area affecting most of the tumor parenchyma. H&E 4x. (d) MSCs+ PEG-HGNs (G4 group). Highly cellular, expansive neoplastic proliferation. H&E 4x. (e) Control tumor (B1 group). Positive staining for Ki-67 on 78% of neoplastic cells. IHQ 10x. (f) MSCs+ PEG-HGNs+ laser treated (B3 group). Positive staining for Ki-67 on 59% of neoplastic cells. IHQ 10x.

The immunohistochemical analysis on the central area of the tumors recovered at the end of the experiment for Ki-67 expression indicated that B2 and B3 tumors exhibited lower expression of the protein when compared to control B1 and B4 tumors (see Supporting Information Table 1), being the difference on the protein expression between B2 and B3, B3 and B1, and B2 and B1, statistically significant ($p<0.05$). Ki-67 is a nuclear antigen expressed only in the different phases of cellular division, and therefore, it is widely used as a

proliferation biomarker to estimate growth rates. In this regard, Ki-67 expression has been proposed as a prognostic indicator of cerebral high-grade glioblastomas[37]. These histological results would suggest the possibility of a better prognosis for tumors subjected to this therapy, especially on the group treated with MSCs+ PEG-HGNs+ laser.

The histological study demonstrated that the liver from B2 and B3 animals presented scattered dark accumulations suggestive of HGNs. These deposits seem to be more abundant in B2. Specific silver staining for HGNs was positive in tumors from B2 and B3, predominantly in the periphery of the neoplastic proliferation. Furthermore, the complete blood count (CBC) analyses did not present any change in all animals.

No histopathological lesions were found in the organs studied (kidney, liver, lung and spleen), denoting the lack of systemic injuries by the proposed localized treatment (Figure 7).

ICP-OES analysis did not detect gold in post mortem analysis of the tumors of the mice administered with HGNs. This is likely due to the fact that, after 27 days (the total number of days from the injection) the nanoparticles were mostly cleared from the tumor site and any remaining gold was under the detection limit of the system (50 $\mu g \cdot L^{-1}$). This represents a very positive result considering that nanoparticles with optimal clearance characteristics will minimize toxicity risks. This result was also not surprising considering that it has been reported that the gold content in the tumor tissue amounts to ≈1 % of its concentration in the injected suspensions[38]. Bioaccumulation in other organs was observed mainly for the B2 animals (animals which received just the IV administration of PEG-HGNs + laser) with a larger accumulation in the liver and the spleen (1.2 and 0.06 ppm, respectively 24h post injection) compared to the B3 animals for which at the same time only 0.024 ppm were detected in the liver. Therefore, a reduced bioaccumulation was observed when using MSCs as carriers of the same nanoparticles. Since both liver and spleen are typical organs where macrophages of the mononuclear phagocyte system reside, the low bioaccumulation for B3 animals is consistent with a scenario where most of the HGNs remain inside MSCs and are therefore not subjected to detection and capture by macrophages. At the experiment end-point gold was not detected in the tumors for both B2 and B3 groups.

Materials and Methods

Synthesis of Hollow Gold Nanospheres. Cobalt chloride hexahydrate (ACS reagent grade), sodium citrate tribasic dihydrate (≥98%), poly(vinylpyrrolidone) (PVP, Mw = 55000 Da), sodium borohydride (≥99%), chloroauric acid trihydrate (ACS reagent grade) and poly(ethylene glycol)methyl ether thiol (SH-PEG; Mw = 1000 Da) were purchased from Sigma-Aldrich. All of these chemicals were used as received. Nanoparticle synthesis was performed following the protocol

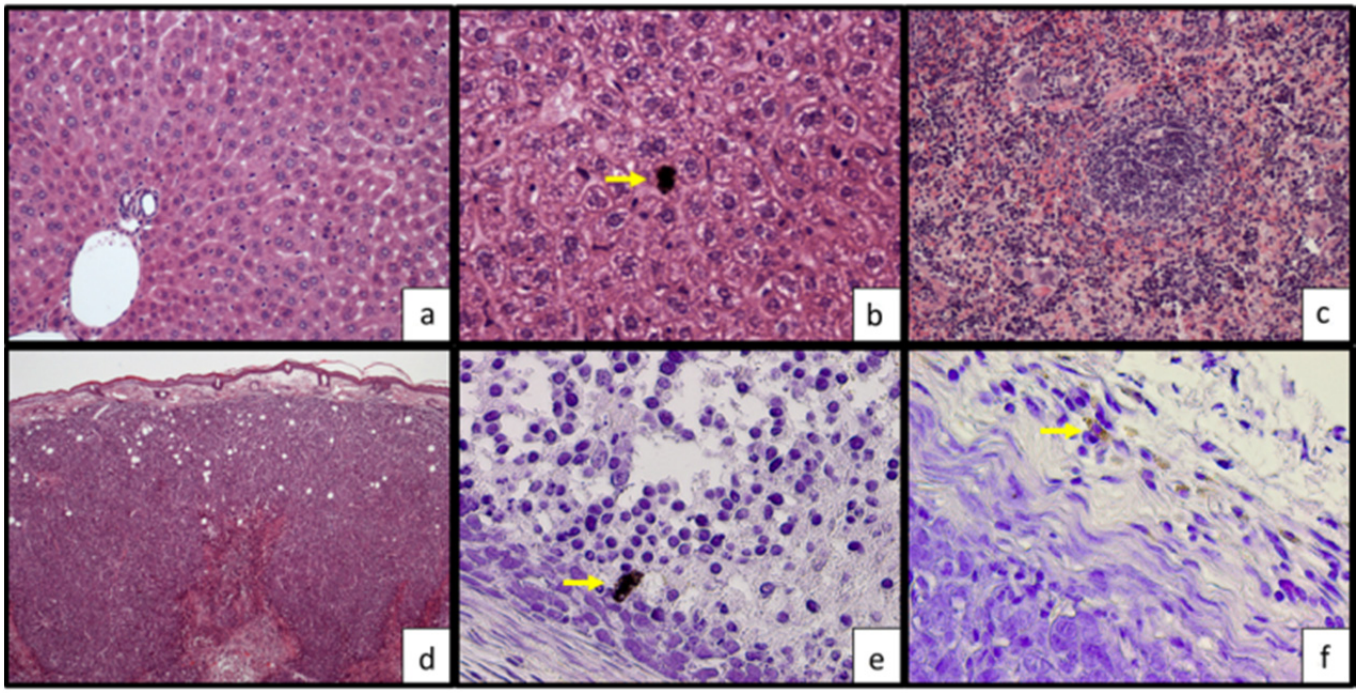

Figure 7. Histological sections recovered at the end of the experiment. (a) Liver (B3 group). Normal liver architecture with hepatocytes arranged in anastomosing plates. Note the regular portal triad. H&E 20x. (b) Liver (B2 group). Note the dark extracellular accumulation within the hepatocytes (arrow). Suggestive of PEG-HGNs deposit. H&E 60x. (c) Spleen (B3 group). The image shows normal organization of the white and red pulps. There are megakaryocytes scattered through the red pulp. H&E 20x. (d) Tumor (B2 group). Expansive highly cellular neoplastic proliferation with a central area of necrosis. H&E 2.5x. (e) Tumor (B3 group). Intracellular positive material (arrow) for the histochemical Silver Stain, compatible with PEG-HGNs deposit 40x. (f) Tumor (B3 group). Intracellular positive material (arrow) for the histochemical Silver Stain, compatible with PEG-HGNs deposit 40x.

described by Preciado-Flores et al.[39] with slight modifications. Briefly, in a two-necked round-bottom flask 400 mL of distilled water, 400 µL of 0.4 M of cobalt chloride hexahydrate ($CoCl_2 \cdot 6H_2O$) and 1.6 mL of 0.1 M sodium citrate trihydrate ($Na_3C_6H_5O_7 \cdot 3H_2O$) were mixed under an inert Ar atmosphere to avoid a premature Co oxidation. After 40 minutes, 2 mL of a 1 wt. % solution of poly (vinylpyrrolidone) (PVP) with an average Mw of 55000 Da and 400 µL of 1.0 M sodium borohydride ($NaBH_4$) were added. The color change from pale pink to brown was indicative of the cobalt nanoparticle formation. Afterwards, 120 mL of distilled water and 180 µL of 0.1M chloroauric acid trihydrate ($HAuCl_4 \cdot 3H_2O$) were mixed with 360 mL of the previous cobalt-based dispersion used as sacrificial template to promote the formation of $CoCl_2$, Co(II) and the reduction of Au^{3+} rendering hollow Au-based shells.

The resulting HGNs were coated with poly-ethylene glycol by using an excess of monofunctional SH-PEG, to take advantage of the strong chemical bond between Au and S[40]. Any excess of unbound PEG was removed by dialysis.

The concentration of the final dispersion was adjusted by centrifugation at 10000 rpm for 10 minutes and both HGNs and PEG-HGNs were thoroughly characterized by transmission electron microscopy (T20-FEI Tecnai thermoionic transmission electron microscopy (TEM)) operated at 200 kV with a LaB6 electron source fitted with a "SuperTwin®" objective lens allowing a point-to-point resolution of 2.4 Å. Elemental analysis was carried out with an EDS (EDAX) detector which allows performing EDS experiments in the scanning mode. Scanning electron microscopy (FEI Inspect F30), and thermogravimetric analysis (TGA; Mettler Toledo TGA/STDA 851e) were also made. Samples were analyzed in Air atmosphere (gas flow 50 mL/min) in a temperature range between 30 and 850 °C with a heating rate of 20 °C/min). UV visible spectroscopy (Jasco V670) was also used in the HGNs characterization.

Cell culture conditions.Murine mesenchymal stem cells (MSCs), HeLa cells and human U251MG glioma cells were obtained from Lonza and Cancer Research-UK cell services, respectively. MSCs were cultured in Dulbecco's modified Eagle's F-12 medium (DMEM F-12, GIBCO) with 10% fetal bovine serum (FBS, GIBCO), 1% penicillin/streptomycin and 1% amphotericin and maintained at 37°C in a 5% CO2-humidified atmosphere under hypoxic conditions (3% O2). For culturing U251MG and HeLa cells Dulbecco's modified Eagle's medium (DMEM, GIBCO) with 10% fetal bovine serum (FBS, GIBCO), 1% penicillin/streptomycin and 1% amphotericin were used under normoxic conditions.

HGNs cytotoxicity evaluation. The Alamar Blue® was the colorimetric assay used to evaluate cell viability and cytotoxicity. This method is based on the reduction of resazurin to resorufin by mitochondrial oxidoreductases. During the evaluation, MSCs were seeded into 96-well culture plates at a concentration of 5 x 10^3 cells per well in 100 µL of the above mentioned medium. After incubation at 37°C in a 5% CO2-humidified incubator under hypoxic conditions for 24 h, the medium was changed to 100 µL of freshly prepared medium enriched with HGNs (5, 10, 20, 50 and 100 µg mL^{-1}) or with PEG-HGNs (20, 50, 100 and 500 µg mL^{-1}) and cells were cultured for another 24, 48 and 72 h. At these different time points cells were washed with PBS and then treated with 10% (v/v) of resazurin dye reagent prepared in DMEM F-12 medium. Culture plates were then placed in a 37°C/5% CO2 incubator under hypoxic conditions for 2 h. Afterwards, fluorescence was evaluated at 530/590 nm excitation/emission wavelengths using a Synergy HT (Biotek) plate reader.

Cellular uptake of nanoparticles. Confocal microscopy characterization (Spectral Confocal Microscope Leica TCS SP2) was carried out to evaluate cellular uptake and trafficking on the cells studied. In this case, cells were seed at a density of 3 x 10^4 cells on 20 mm cover slips (in a 24-well plate) and allowed to grow for 2 days. Then, HGNs (50 µg mL^{-1}) in DMEM F-12 were added keeping the incubation for 1 day. Finally, cells were fixed with para-formaldehyde 4% and stained with phalloidin to label the cytoplasmic actin. HGN-based agglomerates were directly observed by reflection in the confocal microscope without the need of using fluorophores. For obtaining the SEM Dual-Beam (FEI Nova 200 Dual-Beam SEM/FIB) images cells were dehydrated, dyed and embedded in resin before observation. The electronic observation was combined with a focused ion beam (FIB) to visualize and cut the MSCs. Gallium was used as liquid metal ion source to produce cross-sections of the adherent cells. Both the ion column and the electron column operated at accelerating voltages of 30kV.

Flow cytometry. Nanoparticle internalization was evaluated by using flow cytometry. In this case, 5 mL of HGNs or PEG-HGNs (1mg·mL^{-1}) dispersions were maintained under agitation with Rhodamine 123 (1 mg·mL^{-1}, 25µL) for 1 hour. To remove any potential unbound dye, each dispersion was then dialyzed for two days against distilled water. Afterwards, 1 x 10^6 cells were incubated with the corresponding Rhodamine-labeled

nanoparticles and at different time points cells were washed twice with PBS and trypsinized. After centrifugation, cells were resuspended in PBS (1 x 10^6 cells·mL^{-1}) and analyzed by flow cytometry with an ImageStreamX (Seattle, WA, USA).

Cell irradiation. To study the laser effect in the cells containing sub-cytotoxic doses of internalized HGNs, MSCs (50000-100000 cells/well) were incubated with the HGNs (0.02 or 0.05 mg·mL^{-1}) during one day. After that, those adherent cells were washed twice with PBS, to reduce any possible heating potentially produced by free, non-internalized nanoparticles present in the medium. MSCs were then irradiated in DMEM-f-12 during 30 minutes with a NIR laser (808 nm) at 1W·cm^{-2} of irradiance. Then, irradiated cells were incubated in a 37°C/5% CO_2 incubator under hypoxic conditions for 48 h. After that time cells were incubated with the LIVE/DEAD® fluorescent reagent (Life Technologies) following the manufacturer's protocol and visualized under an inverted fluorescence microscope (Olympus IX81). The Alamar Blue® assay was also used in order to compare the viability of the irradiated cells with and without internalized nanoparticles.

In vivo experiments. All procedures were carried out under Project License PI 14/11 approved by the in-house Ethic Committee for Animal Experiments from the University of Zaragoza. The care and use of animals were performed accordingly with the Spanish Policy for Animal Protection RD53/2013, which meets the European Union Directive 2010/63 on the protection of animals used for experimental and other scientific purposes. For these experiments six- to eight-week-old female BALB/c nu/nu mice (Harlan Iberica) were used. All the animals received subcutaneous injections of 5 x 10^6 U251MG cells or HeLa cells suspended in 200 µl of PBS for the generation of subcutaneous xenograft tumors. When the tumor size was >0.5cm^2, the animals were divided into groups of four mice per group.

Two independent experiments were performed in order to assess the efficiency of the photothermal therapy, gold nanoparticles biodistribution and toxicity. In the first experiment, direct intratumoral injections of the nanoparticle-laden cells (HGNs and PEG-HGNs) were used to demonstrate the efficiency of the photothermal therapy, with five experimental groups. In this case, all groups were injected with 5 x 10^6 HeLa cells in one flank of the mouse for tumor induction. Group 1 included control animals which did not receive any treatment; Group 2 included animals that received laser irradiation but not HGNs injection; Group 3 animals received HGNs injection (50 µg) but not laser irradiation. Group 4 animals received HGNs (50 µg nominal dose) carried by 10^6 MSCs and laser irradiation and finally group 5 received a direct injection of HGNs (50 µg) and laser irradiation. After one day of nanoparticle or MSC administration these two last groups and the control group were irradiated with a NIR-laser (808nm) at an irradiance of 1W·cm^{-2} during 5 min. Tumor size was periodically evaluated by using a caliper up to 15 days after irradiation.

The second experiment was aimed to assess the efficiency of MSCs as carriers of HGNs compared to conventional intravenous administration of plasmonic nanoparticles. To this end, we divided the animals into four groups (B1-B4). The first group served as control (B1). The second group (B2) received an intravenous injection of 100 µg PEG-HGNs in 100 µl of PBS through the tail vein. The third (B3) and fourth (B4) groups were injected with a suspension of 1 x 10^6 MSCs separately loaded with 100 µg PEG-HGNs in 100 µL of PBS. Previously, cells were incubated with the PEG-HGNs for 24 hours, and afterwards cells were washed, trypsinized and one million of MSCs containing nanoparticles were injected in the tail vein.

One day after intravenous injection, the second and third groups were irradiated during 5 min with a NIR laser (808 nm) at 1W·cm^{-2} irradiance around all the tumoral area using a spot size larger than the tumor projected surface. The fourth group did not receive any laser irradiation. One week after intravenous injection the same dose of irradiation was used again following the same protocol. Tumor size evolution was evaluated over two weeks, until the tumor size was as big as the maximum size permitted by the University ethics committee. At this time point, animals were euthanized by CO2 inhalation. Tumor, kidney, liver, lung and spleen were collected from each animal for histopathological analysis and to evaluate gold bioaccumulation by ICP-MP-AES (4100, Agilent).

Statistical analysis. All experiments were repeated in triplicate unless otherwise stated. Statistical evaluation of data was carried out using the STATA SE 12 software. To study the statistic differences between groups, a Bonferroni test was carried out. $p<0.05$ was regarded as statistically significant.

Tissue analysis. Tissues were formalin-fixed and processed using routine histological methods. Sections of 3 µm were prepared after paraffin embedding and the slides were stained with hematoxylin and eosin. Microscopic lesions were described and a mitotic activity index was calculated by counting mitotic figures in ten consecutive high-power fields (HPF, 40x) from the most densely packed cellular area of the corresponding sample. To evaluate the proliferation index, an immunohistochemical analysis with Ki-67 (FLEX monoclonal mouse anti-human Ki67 clone MIB-1 from DAKO, Denmark) was performed. Sections were incubated at room temperature with primary antibodies for 20 min at pH 6. The Envision Flex/Hrp Dako™ visualization system was used followed by a counterstaining with hematoxylin. Negative control sections received only antibody diluent instead of the primary antibody. Ki-67 expression was evaluated in all groups by counting positive and negative cells in ten consecutive HPF using the ImageJ software. On those images, the percentage of positive cells and their confidence interval (95%) were calculated. Silver staining (Sigma-Aldrich, Silver Enhancer Kit®) was applied in histological slides of the tumor for detecting HGNs. This staining enlarges the gold colloid label by

precipitation of metallic silver to give a high contrast signal visible under a light microscope.

Organs and tumors were digested by dissolving them in nitric acid during 1 hour at 90°C and hydrogen peroxide for one more hour. Digested samples were diluted and gold content analyzed by ICP-MP-AES (4100, Agilent). Elemental gold standard (TraceCERT®, 1000 mg/L Au in hydrochloric acid, Fluka) was used for calibration.

Conclusions

Hollow gold nanoparticles act as efficient transducers *in vivo* of near infrared light into heat when stereotactically injected into subcutaneous HeLa cell-line xenograft tumors. However, delivering a dose of HGNs to the tumor that is sufficient to achieve the desired thermal effects is challenging when the HGNs are intravenously administered. This was clear in the treatment of subcutaneous U251MG cell-line xenograft tumors, where a poor therapeutic result was obtained for PEG-HGNs injected intravenously in spite of their PEG coating. Two factors are likely contributing to this effect, on the one hand the intrinsic heterogeneity of the EPR effect that leads to a variable distribution of plasmonic nanoparticles within the tumor. On the other, the fact that a significant fraction of the free PEG-HGNs injected intravenously are detected and cleared by RES macrophages, as shown by the gold accumulation found in the spleen and liver of the test animals, reducing the delivery of HGNs to the tumor. Both problems were alleviated by using MSCs as carriers of those nanomaterials.

A successful subcytotoxic internalization of both bare and PEGylated hollow gold nanoparticles was demonstrated in murine MSCs incubated with HGNs under suitable conditions. The HGNs remained inside the cells for at least one week, a period sufficient for the MSCs to reach tumor sites. Taking advantage of the tumor-homing ability of nanoparticle-loaded MSCs, a more homogeneous nanoparticle distribution across the tumoral tissue was obtained and this phenomenon increased the efficiency obtained when applying photothermal therapy on subcutaneous xenograft glioma. The immunohistochemical analysis also confirmed the efficiency of photothermal therapy, especially in those tumors where gold nanoparticles had been delivered by MSCs.

Acknowledgements

Financial support from the EU thanks to the ERC Consolidator Grant program (ERC-2013-CoG-614715, NANOHEDONISM) is gratefully acknowledged.

We are grateful to the Scientific Services of the Aragon Institute of Health Sciences, specifically to the Cytometry and Cell Sorting Services and to the Microscopy and Pathology Services and their specialists: César Vallejo, Javier Godino, Maria Royo, Amparo Gallur, Maria Luisa Bernad and Cyndi Giraldo.

References

1 A. Jemal, F. Bray and J. Ferlay, *A Cancer J. Clin.*, 2011, **61**, 69–90.

2 G. Kucsko, P. C. Maurer, N. Y. Yao, M. Kubo, H. J. Noh, P. K. Lo, H. Park and M. D. Lukin, *Nature*, 2013, **500**, 54–8.

3 J. Li, S. Gupta and C. Li, *Quant. Imaging Med. Surg.*, 2013, **3**, 284–91.

4 S. Kessentini and D. Barchiesi, *Biomed. Opt. Express*, 2012, **3**, 590–604.

5 H. Takagi, K. Azuma, T. Tsuka, T. Imagawa, T. Osaki and Y. Okamoto, *Oncol. Lett.*, 2014, **7**, 1007–1010.

6 E. J. Chisholm, G. Vassaux, P. Martin-Duque, R. C. Vre, O. Lambert, M. Weeks, J. Burnet, I. Peerlinck, B. Pitard, A. Merron, M. S. Dai, G. Alusi, S. J. Mather, K. Bolton, I. F. Uchegbu, A. G. Sehatzlein and P. Baril, *Cancer Res.*, 2009, **69**, 2655–2662.

7 W. Uma Prabhakar, Hiroshi Maeda, Rakesh K. Jain, Eva M. Sevick-Muraca, P. G. Zamboni, Omid C. Farokhzad, Simon T. Barry, Alberto Gabizon and D. C. Blakey, *Cancer Res.*, 2014, **73**, 2412–2417.

8 C. M. Dawidczyk, C. Kim, J. H. Park, L. M. Russell, K. H. Lee, M. G. Pomper and P. C. Searson, *J. Control. Release*, 2014, **187**, 133–144.

9 D. B. Chithrani, *Mol. Membr. Biol.*, 2010, **27**, 299–311.

10 P. L. Rodriguez, T. Harada, D. A. Christian, D. A. Pantano, R. K. Tsai and D. E. Discher, *Science (80-.).*, 2013, **339**, 971–975.

11 K. Matsuo, Y. Ishii, K. Matsuo, T. Yoshinaga, M. Akashi, Y. Mukai, Y. Yoshioka, N. Okada and S. Nakagawa, *Biol. Pharm. Bull.*, 2010, **33**, 2003–7.

12 J. Choi, H.-Y. Kim, E. J. Ju, J. Jung, J. Park, H.-K. Chung, J. S. Lee, J. S. Lee, H. J. Park, S. Y. Song, S.-Y. Jeong and E. K. Choi, *Biomaterials*, 2012, **33**, 4195–203.

13 S.-K. Baek, A. R. Makkouk, T. Krasieva, C.-H. Sun, S. J. Madsen and H. Hirschberg, *J. Neurooncol.*, 2011, **104**, 439–48.

14 M.-R. Choi, R. Bardhan, K. J. Stanton-Maxey, S. Badve, H. Nakshatri, K. M. Stantz, N. Cao, N. J. Halas and S. E. Clare, *Cancer Nanotechnol.*, 2012, **3**, 47–54.

15 U. Steinfeld, C. Pauli, N. Kaltz, C. Bergemann and H.-H. Lee, *Int. J. Pharm.*, 2006, **311**, 229–36.

16 S. Kang, S. H. Bhang, S. Hwang, J.-K. Yoon, J. Song, H.-K. Jang, S. Kim and B.-S. Kim, *ACS Nano*, 2015, **9**, 9678–9690.

17 Y. Liu, M. Yang, J. Zhang, X. Zhi, C. Li, C. Zhang, F. Pan, K. Wang, Y. Yang, J. Martinez de la Fuentea and D. Cui, *ACS Nano*, 2016, **10**, 2375–2385.

18 C. Belmar-Lopez, G. Mendoza, D. Oberg, J. Burnet, C. Simon, I. Cervello, M. Iglesias, J. C. Ramirez, P. Lopez-Larrubia, M. Quintanilla and P. Martin-Duque, *BMC Med.*, 2013, **11**, 139.

19 M. Abad, L. Mosteiro, C. Pantoja, M. Canamero, T. Rayon, I. Ors, O. Grana, D. Megias, O. Dominguez, D. Martinez, M. Manzanares, S. Ortega and M. Serrano, *Nature*, 2013, **502**, 340–345.

20 R. Uchibori, T. Tsukahara, K. Ohmine and K. Ozawa, *Int. J. Hematol.*, 2014, **99**, 377–82.

21 T. Sadhukha, T. D. O'Brien and S. Prabha, *J. Control. Release*, 2014, **196**, 243–251.

22 R. B. B. Borhane Annabi, Ying-Ta Lee, Sandra Turcotte, Emmanuelle Naud, Richard R. Desrosiers, Martin Champagne, Nicoletta Eliopoulos, Jacques Galipeau, *Stem Cells*, 2003, **21**, 337–347.

23 E. K. Mader, G. Butler, S. C. Dowdy, A. Mariani, K. L. Knutson, M. J. Federspiel, S. J. Russell, E. Galanis, A. B. Dietz and K.-W. Peng, *J. Transl. Med.*, 2013, **11**, 20.

24 M. Roger, A. Clavreul, M.-C. Venier-Julienne, C. Passirani, C. Sindji, P. Schiller, C. Montero-Menei and P. Menei, *Biomaterials*, 2010, **31**, 8393–401.

25 R. M. Dwyer, S. M. Potter-Beirne, K. a Harrington, a J. Lowery, E. Hennessy, J. M. Murphy, F. P. Barry, T. O'Brien and M. J. Kerin, *Clin. Cancer Res.*, 2007, **13**, 5020–7.

26 M. R. Loebinger and S. M. Janes, *Thorax*, 2010, **65**, 362–9.

27 A. M. Goodman, Y. Cao, C. Urban, O. Neumann, C. Ayala-Orozco, M. W. Knight, A. Joshi, P. Nordlander and N. J. Halas, *ACS Nano*, 2014, **8**, 3222–3231.

28 B. Díaz, C. Sánchez-Espinel, M. Arruebo, J. Faro, E. de Miguel, S. Magadán, C. Yagüe, R. Fernández-Pacheco, M. R. Ibarra, J. Santamaría and A. González-Fernández, *Small*, 2008, **4**, 2025–34.

29 Y. S. Zhang, Y. Wang, L. Wang, Y. Wang, X. Cai, C. Zhang, L. V Wang and Y. Xia, *Theranostics*, 2013, **3**, 532–43.

30 S. Rao, C. Huang, U. Tata, P. Wu, N. Arora, J. Ahn, V. K. Lin, Y. Hao and J. C. Chiao, *J. Nanotechnol.*, 2014, **2014**, 7.

31 T. Yajima, Y. Yu and M. Futamata, *Phys. Chem. Chem. Phys.*, 2011, **13**, 12454–12462.

32 J. You, R. Zhang, G. Zhang, M. Zhong, Y. Liu, C. S. Van Pelt, D. Liang, W. Wei, A. K. Sood and C. Li, *J. Control. Release*, 2012, **158**, 319–28.

33 J. M. Tucker-Schwartz, K. R. Beavers, W. W. Sit, A. T. Shah, C. L. Duvall and M. C. Skala, *Biomed. Opt. Express*, 2014, **5**, 1731–1743.

34 S. Laurent, S. Dutz, U. O. Häfeli and M. Mahmoudi, *Adv. Colloid Interface Sci.*, 2011, **166**, 8–23.

35 C. Latorre-Romero, M. R. Marin-Yaseli, C. Belmar-Lopez, R. del Moral, P. C. Marijuan, M. Quintanilla and P. Martin-Duque, *Clin. Transl. Oncol.*, 2011, **13**, 10–7.

36 B. R. Smith, E. E. B. Ghosn, H. Rallapalli, J. a Prescher, T. Larson, L. a Herzenberg and S. S. Gambhir, *Nat. Nanotechnol.*, 2014, 1–7.

37 L. Mastronardi, A. Guiducci, F. Puzzilli and A. Ruggeri, *J. Neurosurg. Sci.*, 1999, **43**, 263–270.

38 G. S. Terentyuk, a V Ivanov, N. I. Polyanskaya, I. L. Maksimova, a a Skaptsov, D. S. Chumakov, B. N. Khlebtsov and N. G. Khlebtsov, *Quantum Electron.*, 2012, **42**, 380–389.

39 S. Preciado-Flores, D. Wang, D. a. Wheeler, R. Newhouse, J. K. Hensel, A. Schwartzberg, L. Wang, J. Zhu, M. Barboza-Flores and J. Z. Zhang, *J. Mater. Chem.*, 2011, **21**, 2344.

40 M. Brust, M. Walker, D. Bethell, D. J. Schiffrin and R. Whyman, *J. ChemJournal Chem. Soc. Chem. Commun.*, 1994, 801–802.